THE JOURNAL OF PHYSICAL CHEMISTRY C

Article

pubs.acs.org/JPCC

High-Throughput Investigation of the Geometry and Electronic Structures of Gas-Phase and Crystalline Polycyclic Aromatic Hydrocarbons

Bohdan Schatschneider,*[,†] Stephen Monaco,[†] Jian-Jie Liang,[‡] and Alexandre Tkatchenko[§]

[†]The Pennsylvania State University, Fayette-The Eberly Campus, 2201 University Drive, Lemont Furnace, Pennsylvania 15456, United States

[‡]Accelrys Inc., 5005 Wateridge Vista Drive, San Diego, California 92121, United States

[§]Fritz-Haber-Institut der Max-Planck-Gesellschaft, Faradayweg 4-6, D-14195 Berlin, Germany

Supporting Information

ABSTRACT: The quest for cheap, light, flexible materials for use in electronics applications has resulted in the exploration of soft organic materials as possible candidates, and several polycyclic aromatic hydrocarbons (PAHs) have been shown to be versatile (semi)conductors. In this investigation, dispersion inclusive density functional theory is used to explore all of the current crystalline PAHs within the Cambridge Structure Database (CSD) from both structural and electronic standpoints. Agreement is achieved between the experimental and calculated crystalline structures, as well as the electronic properties. Specifically, variation between the mass densities, unit cell parameters, and intermolecular close contact fractions were within +5%, ±2%, and ±1% of experiment, respectively. It is found that a simple addition of a ∼1 eV constant to the DFT-PBE gaps provides good agreement with the experimental optical gaps of both gas phase (within ±2.6%) and crystalline (within ±3.5%) PAHs. Structural and electronic analysis revealed several correlations/trends, where ultimately limits in the band gaps as a function of structure are established. Finally, analysis of the difference between band gaps of the isolated molecules and crystals ($\Delta E_g^{Xtal-Mol}$) demonstrates that $\Delta E_g^{Xtal-Mol}$ can be captured qualitatively by PBE and PBE0 functionals, yet significant quantitative deviations remain between these functionals and experiment.

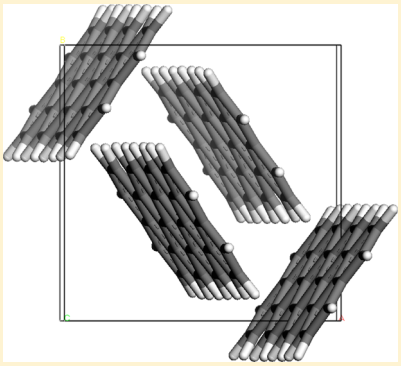

1. INTRODUCTION

The quest for inexpensive, flexible, lightweight materials for use in electronic applications has led researchers to explore what useful arrays can be constructed through organic means, and the ability to predict useful properties within organic−electronic materials is quickly becoming an essential part of organo-electronic product design. Polycyclic aromatic hydrocarbons (PAHs) make up a group of organic molecular crystals (OMCs) that have shown promise for use in electronics and electro-optics.[1,2] Despite their versatility and abundance, theoretical exploration of the electronic properties of most crystalline PAHs remains uncharted. Here we use dispersion inclusive density functional theory (DFT) to shed light onto the structural and electronic trends occurring within this promising group of materials.

The topology of individual PAH molecules can be classified as (1) linear/nanoribbons (comprised of homologous groups of oligoacenes, phenacenes, and oligorylenes), (2) circular flakes/discs (K-region PAHs and circumacenes), and (3) triangular. Within each topology two edge/periphery types exist: (1) zigzag and (2) arm-chair. In general, it is known that in a given topology of PAHs (as well as nanoflakes) that the size of the band gap (E_g) decreases[3−5] as the number of aromatic rings (carbon atoms) increases, where arm-chair edge PAHs have larger band gaps and cohesive energies (enthalpies of formation) than their zigzag counter parts. Similar trends can also be found in fully benzenoid PAHs.[5] It is then understood that the ionization energy (I) decreases and the electron affinity (A) increases with increasing number of rings in a homologous class[4] (this follows from the above E_g-trend as the fundamental/transport gap is $I - A$).[6] It is also recognized that as the number of edge atoms (N_s) increase with respect to the total number of atoms (N), the cohesive energy decreases.[3]

Traditionally, PAHs can be either heterocyclic or only carbon containing and assemble in molecular crystalline arrays under ambient conditions. Those PAHs containing only hydrogen and aromatic carbon can be classified into five crystalline motifs, definable by the π^0-parameter (a product of the interplanar angle between molecular components and the fraction of C···C intermolecular close contacts[7]). The five motifs, (a) herringbone (HB), (b) sandwich-herringbone (SHB), (c) β-herringbone (β-HB), (d) γ, and (e) β are depicted in Figure 1a−e using structures that exemplify the characteristics of each motif.[8,9]

Received: June 28, 2014
Revised: August 7, 2014
Published: August 7, 2014

   dx.doi.org/10.1021/jp5064462 | J. Phys. Chem. C 2014, 118, 19964−19974

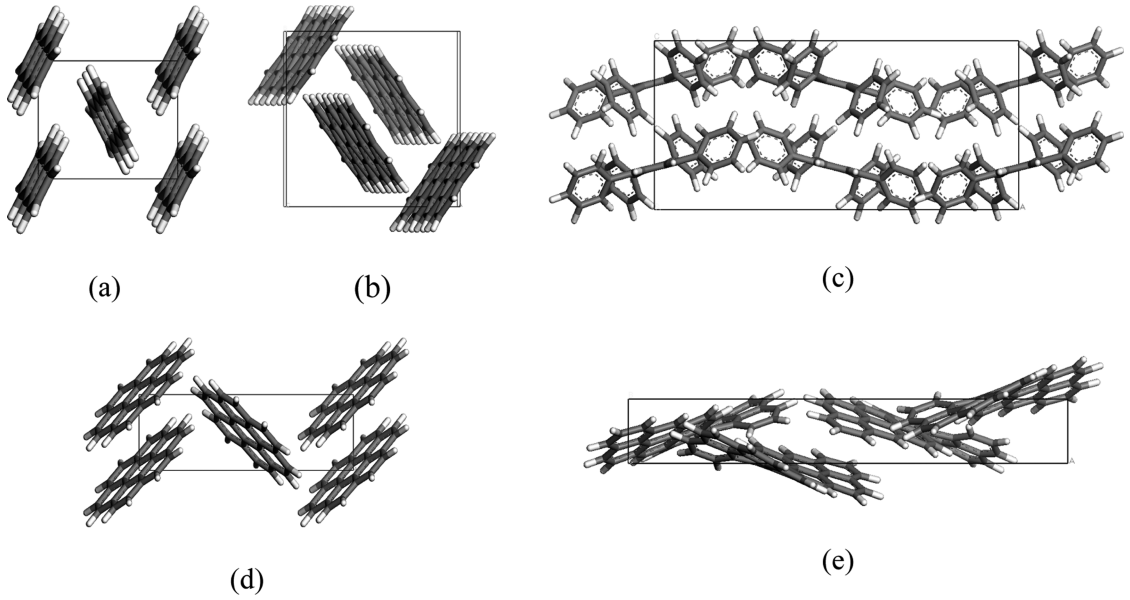

Figure 1. PAH motifs. (a) HB, anthracene [ANTCEN]. (b) SHB, quaterylene [QUATER10]. (c) β-HB, 1,2,3,4-tetraphenylbenzene [FOVVOB]. (d) γ, coronene [CORONE01]. (e) β, anthra[2,1,9,8-*hjkl*]benzo[de]naphtha[2,1,8,7-*stuv*]pentacene [BOXGAW].

Each motif has characteristic amounts of C···C (π···π), C···H, and H···H intermolecular close contact interactions.[7−10] It is known that the HB and β-HB structures are heavily dependent on C···H close contact interactions for crystal stabilization as calculated via Hirshfeld surface analysis[7] but get the least amount of crystal stabilization from C···C close contacts on average compared with other motifs. The SHB structures are dependent on C···H interactions as well but become increasingly dependent on C···C interactions compared with the HB and β-HB motifs because half of each molecular component is involved in π···π stacking interactions. The β and γ motifs are the most dependent on C···C interactions because the large molecular components have low N_s/N ratios (compared with other motifs), providing ample π-orbitals for stacking interactions.

Despite the extensive knowledge of gas phase PAH band gap trends, little is known about the band gap vs structural/motif dependence in crystalline PAHs. We previously investigated the oligoacenes[11,12] (a prototypical group of PAHs) in great detail using dispersion inclusive density functional theory. In those studies (as well as others[13,14]), we benchmarked the Tkatchenko−Scheffler dispersion energy method (PBE+vdW) for structural and property predictions of molecular crystals with a specific aim on the larger PAH family. The oligoacene investigations mentioned above demonstrated that PBE+vdW can provide excellent structural agreement with experiment, as well as accurately model the pressure induced structural changes of naphthalene, anthracene, and pentacene. PBE +vdW was also used to reproduce the pressure induced phase transition of tetracene along with the pressure induced changes to the HOMO−LUMO band gaps of tetracene and pentacene. With the aforementioned success in mind, we set our sights on investigating the structural and electronic trends of all 91 PAHs currently in the Cambridge Structural Database (CSD) in order to gain further chemical insight into this unique class of crystals.

2. METHODOLOGY

All PAHs investigated in this study are listed in Table S1 of the Supporting Information. Experimental X-ray structures were acquired as referenced in the CSD (reference codes have been provided). Structure searches were conducted using CSD version 5.32 via Conquest version 1.3 with the following search criteria selected: 3D coordinates determined, not disordered, no errors, not polymeric, no ions, no powder structures, and only organics. All selected PAH structures contain only hydrogen and aromatic carbon atoms. Structures were limited to carbon and hydrogen atoms because other elements can have significant effects on the electronic and structural properties. Crystal Explorer 3.0[15] was used to generate the Hirshfeld surfaces and corresponding fingerprint plots.

Density functional theory with dispersion interactions was utilized in the CASTEP program for the optimization of the PAH crystal structures using the Perdew−Burke−Ernzerhof exchange-correlation functional (PBE)[16] with the Tkatchenko−Scheffler dispersion energy method (+vdW),[17] where the cost of the TS-vdW energy is negligible compared with the underlying DFT calculation. The convergence criteria and methods used for calculating all crystalline PAH structures and band gaps were as described in previous investigations of oligoacenes.[11] Isolated molecular band gaps (E_g^{Mol}) were also calculated in CASTEP using the same convergence criteria as used for the crystals except the E_g^{Mol} were calculated on the optimized molecules using only Γ point. Molecules were placed in a periodic cell with a minimum of 10 Å to the cell boundary before geometry optimization.

Band gaps were obtained without dispersion correction as the fully self-consistent implementation of the PBE+vdW method (i.e., where the potential due to vdW interactions enters self-consistently in the solution of the Kohn−Sham equations), which leads to negligible modifications of electronic properties for molecular crystals. For example, for benzene and naphthalene crystals, the band gap modifications amount to only a few tenths of a millielectonvolt.

The long-range van der Waals energy was determined from the TS-method; that is, the difference between the PBE total energy and the dispersion corrected total energy. The entire set of calculations and corresponding analyses were automated

dx.doi.org/10.1021/jp5064462 | J. Phys. Chem. C 2014, 118, 19964−19974

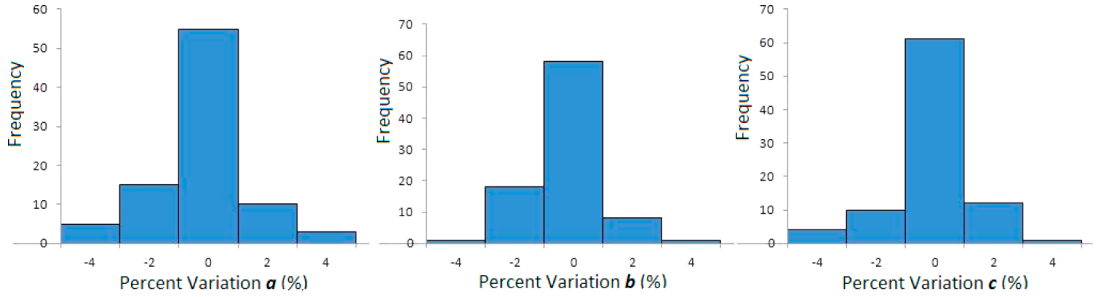

Figure 2. Histograms of percent variation between PBE+vdW and experimental unit cell parameters for 91 PAHs. Negative numbers indicate the calculated unit cell parameters are smaller in the given cell dimension.

through PERL scripting. Problem structures (outliers) were addressed separately and recalculated.

3. RESULTS AND DISCUSSION

3.1. Structural Analysis. The first step in establishing a computational method for use in a high-throughput scenario is to establish its reliability for calculating structural properties.[18,19] Good agreement between the experimental and calculated crystal structures is demonstrated in Figures 2−4. The percent variation between the experimental and calculated unit cell parameters is shown in Figure 2, where the majority of the calculated unit cell parameters are within ±2% of experiment.

Comparison of the experimental and calculated densities is provided in Figure 3. Nearly all of the geometry optimized

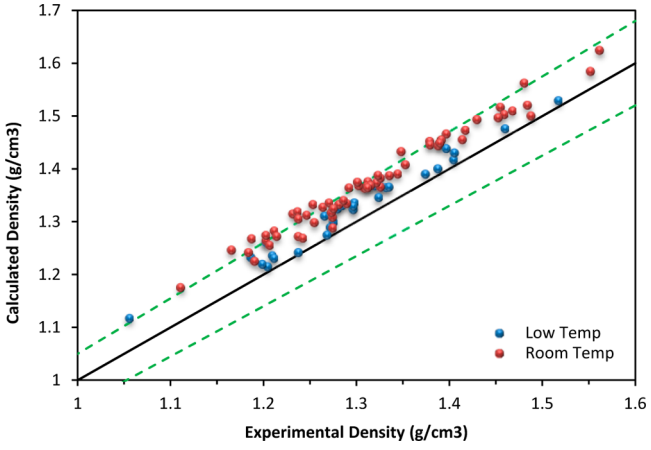

Figure 3. Comparison of calculated and experimental densities for 91 PAHs. Black line represents exact agreement between experiment and calculation. Green dotted lines represent ±5% variation. Red balls are structures obtained at room temperature, and blue balls are structures obtained below room temperature. Calculated structures more than +5% from experiment have structure numbers from Table S2 in the Supporting Information of 2−5, 7, 16−18, 27, 30, 34, 35, 39, 42, 43, 45, 57, 63, 77, 82, and 87.

structures (run at 0 K) are denser than experiment. One reason for the difference is that most of the PAH X-ray studies were conducted at room temperature, leading to lower densities than those calculated at 0 K (see Supporting Information Table S2). Despite the temperature difference between calculation and experiment, ∼77% of the calculated densities are within +5% of experiment (indicated by green lines in Figure 3). When the X-ray structures were determined at lower temperatures (<273 K), variation decreases to within +2.3% on average. Some calculated structures corresponding to room temperature X-ray structures were more than +5% as dense; however no obvious phase/motif transitions were observed via analysis of the space group or the π^0-parameter[7] for these structures.

To assess the geometry within the unit cell, a quantitative, whole-molecule comparison of the intermolecular close contacts was performed from the breakdown of fingerprint plots constructed via the deconvolution of the Hirshfeld surface. Fingerprint plots provide two-dimensional depictions of the Hirshfeld surface plotted as a function of distance between the interior and exterior nuclei and a point on the Hirshfeld surface. Fingerprint plots can be decomposed according to select atom−atom contacts, providing a quantitative measure of the intermolecular contact fractions occurring at the surface. For a full description of Hirshfeld surface analysis and its possible applications for understanding intermolecular interactions within molecular crystals, we refer the reader to our previous work[7,11,13] and several encompassing reviews and technical discussions.[10,15,20]

Figure 4 shows that agreement is achieved between the calculated and experimental intermolecular close contact fractions when PBE+vdW is used for structure prediction. The slightly increased C···H and decreased H···H close contacts in the calculated structures compared with those of experiment in Figure 4 are a reflection of the increased densities in the calculated structures (resulting in more efficiently packed arrays). This observation is consistent with the fact that lowering the temperature of PAHs will have similar effects as applying pressure; that is, increasing the densities and rearranging the intermolecular close contacts. More specifically, when PAHs (oligo(*para*-phenylenes),[21] oligoacenes,[11,22,23] and heterocyclic[13] structures) are placed under pressure, the interplanar angle increases to increase the $\pi\cdots\pi$ interactions. The increased interplanar angle and $\pi\cdots\pi$ interactions have been shown to increase the C···C and C···H interactions while decreasing the H···H contacts.[7,13] These same effects also surface when the temperature of PAHs is decreased (at ambient pressure).

There is one notable outlier in Figure 4, namely, DBPERY of the γ-motif. In the case of DBPERY, there is compression of the unit cell parameters (a, b, and c), a +4.1% change in density, and a small alteration (∼0.4°) of the interplanar angle (θ) with respect to experiment. These structural changes cause the outlying intermolecular interaction behavior, yet no motif or phase transition was observed.

Comparison of the C···C intermolecular close contacts ($\pi\cdots\pi$ stacking) and the density of the experimental structures extracted from the CSD shows that a direct relationship exists for PAHs (see Figure 5a). The average densities of each motif

dx.doi.org/10.1021/jp5064462 | J. Phys. Chem. C 2014, 118, 19964−19974

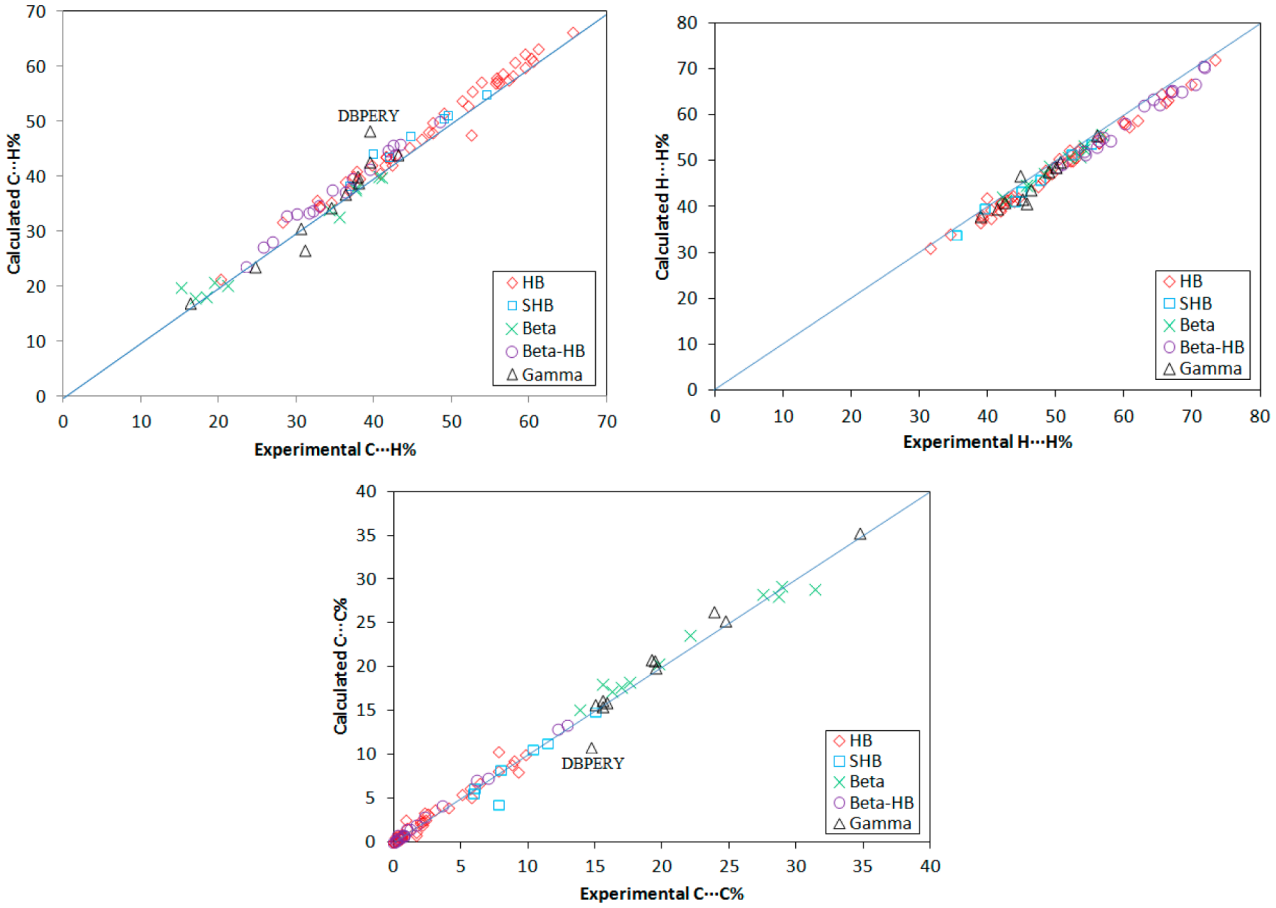

Figure 4. Comparison of intermolecular close contact fractions between calculated and experimental structures as derived via Hirshfeld surface analysis. Blue line represents exact agreement between experiment and DFT. Values for individual PAHs are available in Supporting Information Table S3.

in Figure 5a proceed from the least dense HB/β-HB structures, to SHB structures, followed by the densest, γ and β structures. A linear best fit of the data in Figure 5a shows that ∼90% of PAH mass densities are within ±5% of the line. Extrapolation of the best fit line to 100% C···C interaction (as in the case of graphite) results in a density of 2.154 g/mL. This density is in agreement with that of graphite flakes (2.144 g/mL)[24] and within ∼5% of highly orientated pyrolytic graphite (HOPG, 2.266 g/mL[25]).

When the long-range vdW dispersion energy per atom (including contributions from both hydrogen and carbon) is plotted as a function of density for the optimized structures, it can be seen that the vdW contribution to the crystal stabilization increases as a function of the density (see Figure 5b). Also, the average vdW energy per atom (E_{vdW}) increases similarly to the density with respect to motif in Figure 5b; that is, the HB/β-HB structures have the least E_{vdW}, with the SHB structures having more, followed by the γ and β structures (which are densest) containing the highest E_{vdW} contributions to crystal stability. A linear fit of the data in Figure 5b shows that 98% of the data is within ±5% of the line. When the best fit line is extrapolated to a density of 2.266 g/mL (that of HOPG), the vdW energy per atom is −0.14 eV/atom. When HOPG is geometry optimized using PBE+vdW under the same convergence criteria, E_{vdW} is also −0.14 eV/atom.

The relationship between the C···C intermolecular close contacts and the E_{vdW} as calculated from the geometry optimized structures is shown in Figure 5c. Here, a direct relationship is observed between the C···C interactions and the average E_{vdW}. Extrapolation of the best fit line in Figure 5c to 100% C···C% results in a E_{vdW} of −0.136 eV/atom; the same E_{vdW} as calculated from PBE+vdW and the best fit line equation of Figure 5b when the density is 2.21 g/mL (ρ of graphite). It is uncanny that the linear fits in each of these figures, when extrapolated, result in values associated with an infinite PAH array, namely, graphite. In addition, while the entire stabilization of the crystalline structure due to long-range vdW contributions does not come from just the C···C interactions, an increase in the C···C contacts (or π···π interactions) can have up to a ∼30% stabilizing effect on PAH matrices when one compares, for example, HB structures with those of γ and β arrangements.

To sum up the trends present in Figure 5, in can be said that the densest PAHs will have the largest vdW stabilization energies and most prevalent amount of C···C contacts (or π···π interactions).

3.2. Electronic Properties. Previously, we calculated the structures and fundamental band gaps (E_g^{fun}) of crystalline oligoacenes, from naphthalene (2A) to pentacene (5A).[11] In that study, and others,[27,28] it was shown that the Kohn−Sham gap (E_g^{KS}) could correctly predict the trend of decreasing E_g with increasing number of rings but that quantitative prediction of E_g^{fun} (I-A) using KS-orbitals led to severe underestimations due to the inherent physical differences existing between E_g^{KS} and E_g^{fun}. While E_g^{KS} should not be used to predict E_g^{fun}, it is been shown to be an excellent tool for the prediction of the optical

dx.doi.org/10.1021/jp5064462 | J. Phys. Chem. C 2014, 118, 19964−19974

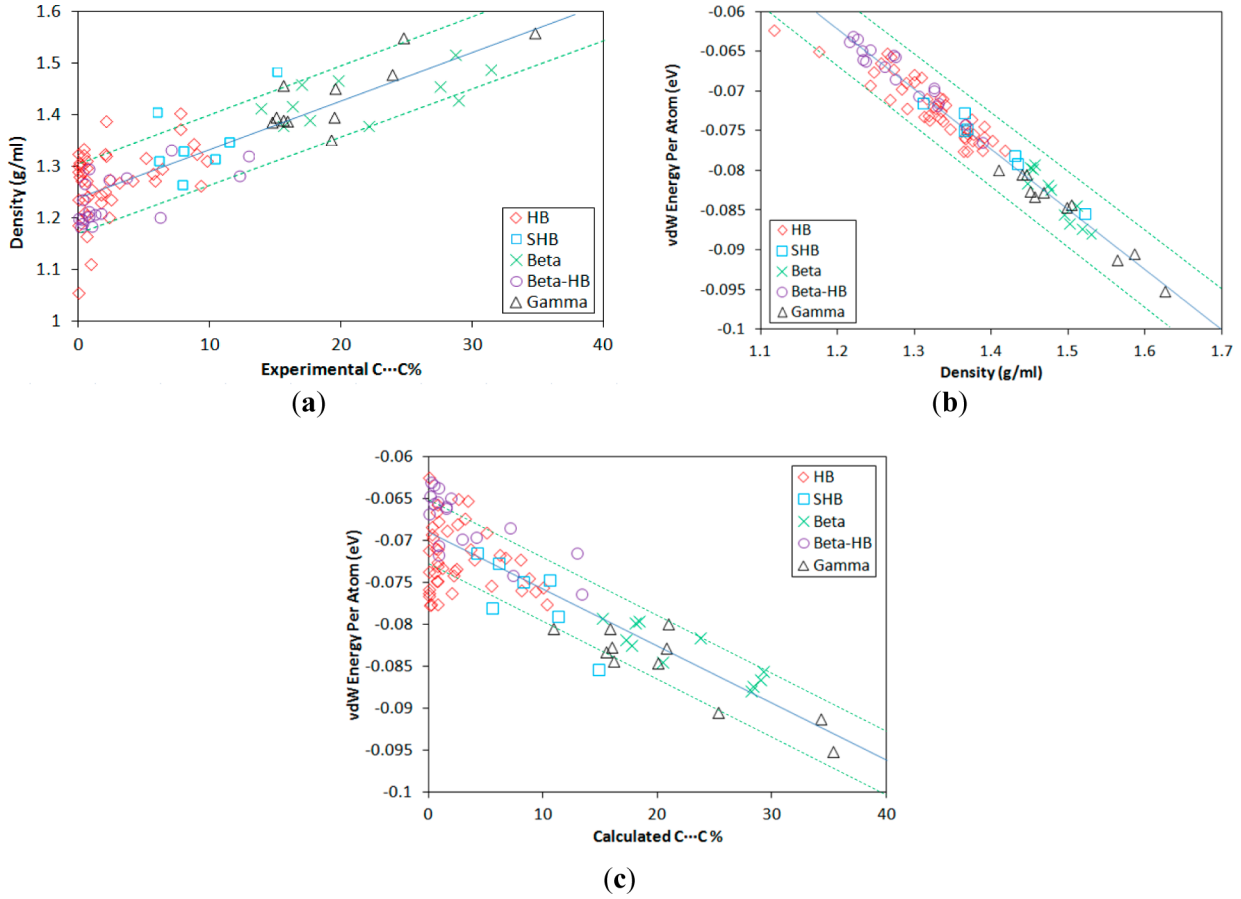

Figure 5. (a) Density as a function of C···C intermolecular close contact fractions from experimental PAH structures (as extracted from CSD). Blue line is a linear best fit to the data (ρ = 0.0091 g/mL (C···C%) + 1.2435 g/mL) and the green lines indicate ±5% from the best fit line. (b) van der Waals energy per atom as a function of density. Values obtained from optimized structures. Blue line is a linear best fit to the data (E_{vdW} = −0.072 eV·mL/g (ρ) + 0.0234 eV). (c) van der Waals energy per atom as a function of the C···C intermolecular close contact fractions. Values obtained from optimized structures. Blue line is a linear best fit to the data (E_{vdW} = −0.000661 eV·(C···C%) − 0.0694 eV).

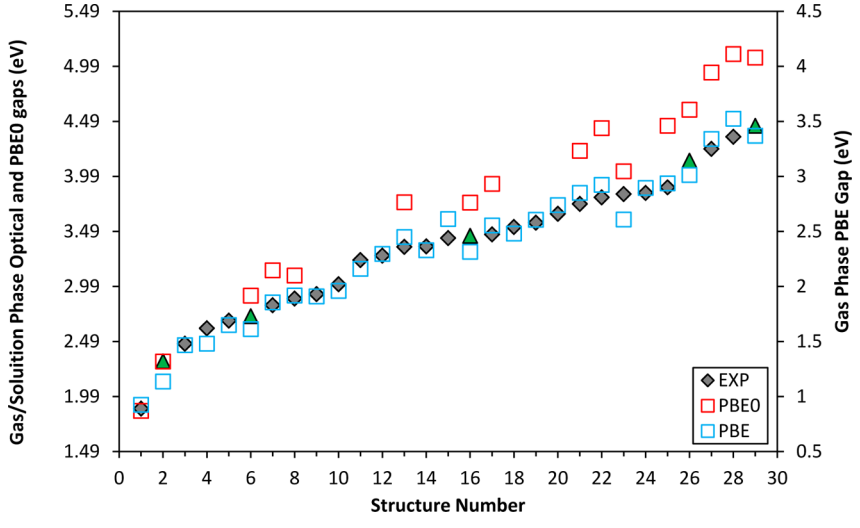

Figure 6. Comparison of predicted and experimental gas/solution phase optical gaps for select PAHs. E_g^{opt} and E_g^{PBE0} are on the primary axis. E_g^{opt} are as referenced in Table 1 (green triangles are gas phase and gray diamonds are solution phase). E_g^{PBE} are plotted on the secondary vertical axis (on the right) and aligned with experimental values (see details in the text) by shifting the zero crossing of the secondary vertical axis by 0.99 eV relative to that of the primary axis (same scale as the primary axis). Structure reference numbers correlate with Table 1.

gap (E_g^{opt}), expanded upon below. In order to gain insight into the electronic properties of the entire class of PAHs in a high-throughput manner, E_g^{opt} values of gas/solution phase and crystalline PAHs were explored via prediction with E_g^{KS}.

dx.doi.org/10.1021/jp5064462 | J. Phys. Chem. C 2014, 118, 19964−19974

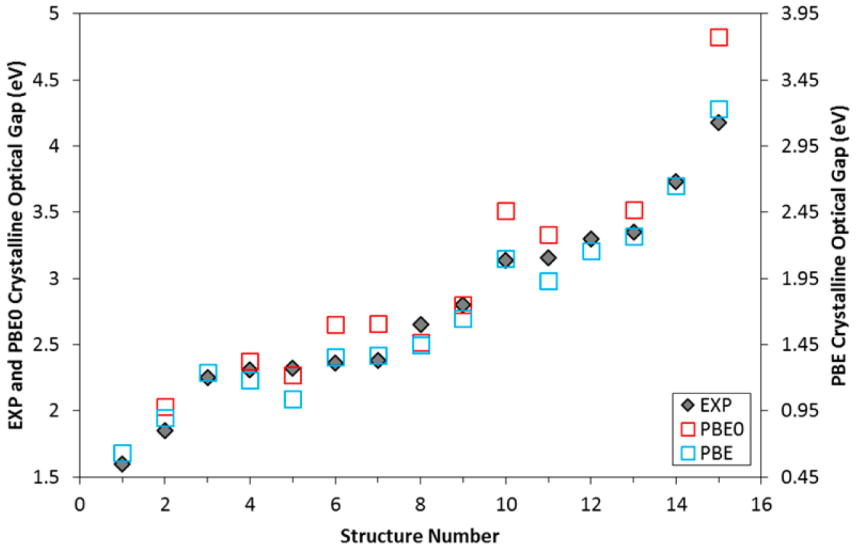

Figure 7. Comparison of predicted and experimental optical gaps of crystalline PAHs. Experimental and PBE0 gaps are on the primary axis. Experimental gaps are as referenced in Table 2. PBE gaps are plotted on the secondary vertical axis (on the right) and aligned with experimental values by shifting the zero crossing of the secondary vertical axis by 1.05 eV relative to that of the primary axis (same scale as the primary axis). Structure reference numbers correlate with Table 2.

Experimental optical gaps (E_g^{opt}) of the PAHs were obtained from the *p*-bands of their optical spectra (standard practice for PAHs).[5,29] For solution spectra, solvent constants were added to account for solvent stabilization effects.[29] It is noted that acquisition of the E_g^{opt} of crystalline PAHs is technically challenging because one must obtain the optical excitation of extremely thin crystals or films due to the materials' large extinction coefficients. Furthermore, intermolecular coupling can be large enough in PAHs that exciton and charge transfer states can dominate the spectral features, in addition to polarization and temperature effects.[30−32] For these reasons, E_g benchmarking of crystalline PAHs can be difficult with predictive methods, and this may be why previous large scale PAH investigations[3,4,33−36] were only performed on gas phase molecules.

The E_g^{opt} is defined as the energy needed for electronic transition of one electron from (1) the HOMO to LUMO energy levels in molecules or (2) the valence to conduction bands in solids where little distance exists between the electron−hole pair (bound excitonic state). While optical spectroscopy is typically used to establish E_g^{opt}, recent work[4,63,64] shows that the calculation of E_g^{KS} (from either *exact* or approximated (GGA, LDA) models) can provide reliable physical and quantitative representation of this phenomena. While E_g^{KS}, the difference between the highest occupied one electron state and the lowest unoccupied one, for molecules in the gas phase has been shown to reliably predict E_g^{opt}, application to extended solid networks has met with significant scrutiny. However, it is expected that in *molecular* solids bound by weak intermolecular interactions (such as PAHs) that E_g^{KS} could predict E_g^{opt} as in the "normal" molecular situation because strongly bound Frenkel excitons remain localized within the excited molecule.[63]

Regardless of the aforementioned difficulties and successes, Figures 6 and 7 and Tables 1 and 2 show that E_g^{KS}, calculated using PBE (E_g^{PBE}), does an excellent job of predicting the *relative* optical gaps of PAHs in both the gas and crystalline phases. Interestingly, it appears that for PAHs, an accurate value of the E_g^{opt} may be obtained by simply adding a constant of ∼1 eV (here on called, ξ_{PBE}) to E_g^{PBE} regardless of phase. Specifically, ξ_{PBE} is 0.99 eV for solution/gas phase comparison

Table 1. Predicted and Experimental Gas/Solution Phase Optical Gaps of Select PAHs[a]

CSD code	structure number	motif	mol E_g^{PBE}	mol E_g^{PBE0}	mol E_g^{opt}
QUATER10	1	SHB	0.93	1.86	1.88[4]
PENCEN[b]	2	HB	1.14	2.31	2.31[4,28]
POBPIG	3	HB	1.47		2.47[37]
QQQCIG04	4	HB	1.48		2.51[38]
CORXAI10	5	β	1.65		2.68[39]
TETCEN01[b]	6	HB	1.61	2.91	2.71[4,29,34]
PERLEN07	7	SHB	1.86	3.14	2.82[4,5]
OVALEN01	8	γ	1.92	3.09	2.88[4]
TBZPER	9	β	1.91		2.92[40]
DBPERY	10	γ	1.96		3.01[41]
TBZPYR	11	β	2.16		3.23[40]
DBZCOR	12	γ	2.30		3.27[41]
HBZCOR	13	γ	2.45	3.76	3.35[5,41]
BNPERY	14	SHB	2.33		3.35[41]
TEBNAP	15	β -HB	2.61		3.43[29]
ANTCEN[b]	16	HB	2.32	3.75	3.45[4]
WOQPAT	17	γ	2.56	3.92	3.46[5]
BEANTR	18	HB	2.48		3.53[29]
DBNTHRO02	19	HB	2.61		3.57[29]
CEQGEL	20	SHB	2.74		3.65[40]
CORONE01	21	γ	2.85	4.22	3.74[4]
ZZZOYC01	22	HB	2.92	4.43	3.80[4,5]
PYRENE02	23	SHB	2.61	4.04	3.83[40]
BZPHAN	24	HB	2.90		3.84[29]
CRYSEN01	25	HB	2.94	4.45	3.89[4]
CORANN12[b]	26	HB	3.01	4.60	4.13[5]
PHENAN	27	HB	3.34	4.93	4.24[4,29]
TRIPHE12	28	HB	3.53	5.10	4.36[5,29]
NAPHTA04[b]	29	HB	3.37	5.07	4.45[4]

[a] E_g in units of eV. All PBE/PBE0 gaps were calculated from PBE +vdW geometry optimized structures. See Supporting Information Table S1 for molecule names. [b] Indicates gas phase.

dx.doi.org/10.1021/jp5064462 | J. Phys. Chem. C 2014, 118, 19964−19974

Table 2. Predicted and Experimental Optical Gaps of Select Crystalline PAHs[a]

CSD code	structure number	motif	crystal E_g^{PBE}	crystal E_g^{PBE0}	crystal E_g^{opt}	other E_g^{opt} values
QUATER10	1	SHB	0.63		1.60[42]	1.7[43]
PENCEN	2	HB	0.90	2.03	1.85[28]	1.8
POBPIG	3	HB	1.24		2.25[44]	2.28[45]
QQQCIG14	4	HB	1.18	2.38	2.31[46]	
QQQCIG04	7	HB	1.04	2.27	2.32[48]	
QQQCIG13	5	HB	1.36	2.65	2.36[46]	
TETCEN01	6	HB	1.37	2.66	2.38[30,47]	
PERLEN07	8	SHB	1.45	2.52	2.65[49]	2.61,[50] 2.67[51]
HBZCOR	9	γ	1.65	2.80	2.80[52]	
BEANTR	10	HB	2.10	3.514	3.14[53]	
ANTCEN	11	HB	1.93	3.33	3.16[31]	
PYRENE02	12	SHB	2.16		3.30[54]	
CORONE01	13	γ	2.27	3.52	3.35[55]	
TERPHEN02	14	HB	2.65		3.73[56]	
BIPHEN	15	HB	3.23	4.826	4.18[57]	

[a] E_g in units of eV. All PBE/PBE0 gaps were calculated from PBE+vdW geometry optimized structures. See Supporting Information Table S1 for structure names.

while ξ_{PBE} is 1.05 eV for the crystalline phase. The addition of ξ_{PBE} results in calculated gaps that differ from E_g^{opt} by only ±2.6% on average for the isolated molecules and ±3.5% on average for the crystalline ensembles. The single parameter fit to the PBE gap is a welcomed finding because E_g calculations utilizing PBE are an order of magnitude cheaper compared with E_g calculations using more "precise" methods such as hybrid functionals like PBE0,[11] HSE03,[11] and B3LYP[4] or quasiparticle corrections[28] and time-dependent methods.[4]

It is also interesting to note that the PBE method can distinguish between the optical gaps of different polymorphs. This can be seen in Table 2 and Figure 7 for the case of monoclinic (QQQCIG13), triclinic (QQQCIG14), and orthorhombic (QQQCIG04) rubrene. Here the subtle differences in molecular packing lead to differences in the optical spectra of each polymorph, which are captured by PBE.

Calculation of E_g^{opt} using the hybrid PBE0 functional (E_g^{PBE0}) resulted in values that agreed reasonably with experimental E_g^{opt} for the gas phase (within +12% on average), while better agreement was found to exist for the crystalline band gaps (within ±5.6% on average). Though the PBE0 calculations are parameter free, they come at *significant* additional cost to that of PBE and result in larger errors compared with the adjusted PBE gaps. Furthermore, the incorporation of Hartree−Fock orbitals into the PBE0 band gap calculation changes the physical meaning of the numerical value compared with PBE; that is, it is known that hybrid functionals are a better assessment of E_g^{fun} as opposed to E_g^{opt};[63] that is why E_g^{PBE0} is (nearly) always larger than E_g^{opt} in Figures 6 and 7. The reason that E_g^{PBE0} is closer to E_g^{opt} in the crystalline case (Figure 7) than in the gas phase is simply because the E_g^{fun} and E_g^{opt} have nearly the same value in crystals as a result of exciton delocalization and dielectric screening effects.[28,63]

A comparison of two sets of *calculated* gaps is shown in Figure 8: one set based on the experimental structures and the other on the geometry optimized structures. It can be seen that the experimental room temperature structures produce larger gaps than the geometry optimized structures ~96% of the time, but that the values from both sets are within ±5% on average. This difference occurs because the calculated structures are optimized at 0 K, while the experimental structures were all obtained at temperatures above 100 K. This difference in

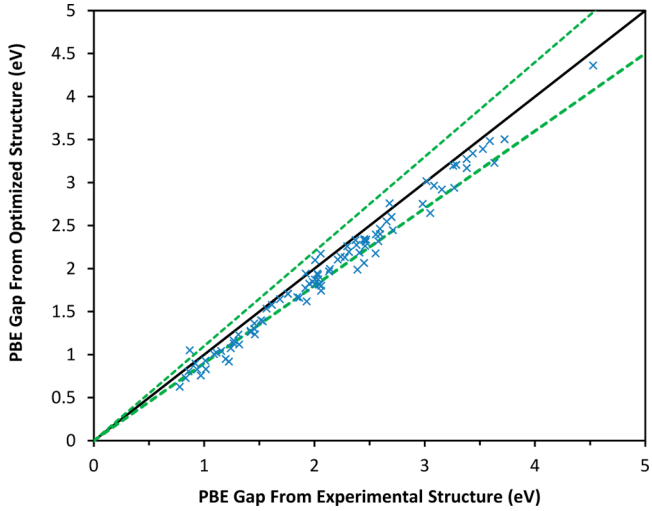

Figure 8. DFT-PBE gaps from the geometry optimized and the experimental structures. Gaps were calculated on PBE+vdW geometry optimized structures and experimental structures as extracted from the CSD. Black line represents exact agreement between experiment and DFT while the green dotted lines represent ±5% variation.

thermal conditions results in variations in the densities (ρ), and consequently intermolecular interactions. Ultimately, the denser PBE+vdW optimized structures have smaller band gaps than the high-temperature experimental counterparts (the band gap density dependence is expanded upon in section 3.3 where we show that increased ρ results in smaller E_g values).

3.3. Structure and Band Gap. It is useful to have property trends and limits to guide the design of new materials, and in this section, we demonstrate that limits exist in the possible optical gaps of PAH crystals as a function of the crystalline structure. The relationship between the intermolecular close contact fractions as obtained via Hirshfeld surface analysis and the predicted E_g^{opt} is shown in Figure 9. The C···C interactions are shown to have an inverse relationship with the maximum possible E_g^{opt} in Figure 9a. It is interesting to note that if the optical gaps and C···C% of the two PAH extrema, namely, benzene and graphite, are used to create a boundary line, all PAH optical gaps will exist below this limit (see Figure 9a). In contrast to the inverse relationship of Figure 9a, Figure 9b

dx.doi.org/10.1021/jp5064462 | J. Phys. Chem. C 2014, 118, 19964−19974

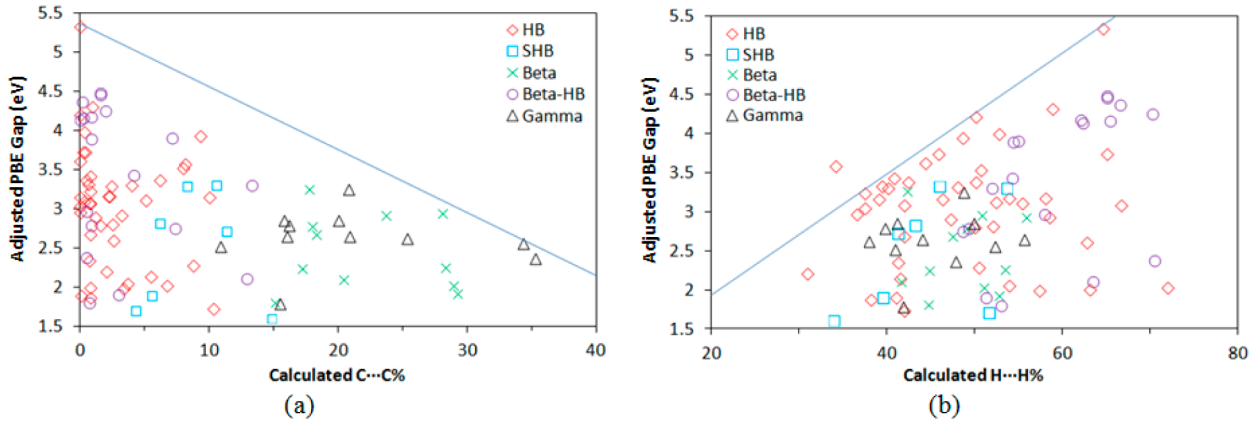

Figure 9. Comparison of predicted optical gaps and intermolecular close contact fractions for geometry optimized structures. E_g^{PBE} in both panels a and b were calculated on PBE+vdW geometry optimized structures and adjusted with ξ_{PBE} to give the predicted E_g^{opt}. (a) C···C close contact fractions vs E_g^{opt}. Blue line represents an E_g^{opt} boundary as a function of C···C%. E_g^{opt} and C···C% of BENZEN (5.342 eV, 0%) and graphite (0.04 eV,[58] 100%) were used for boundary construction. (b) H···H close contact fractions vs E_g^{opt}. Optical gaps and H···H% of BENZEN (5.342 eV, 64.6%) and graphite (0.04 eV,[58] 0%) were used for boundary construction.

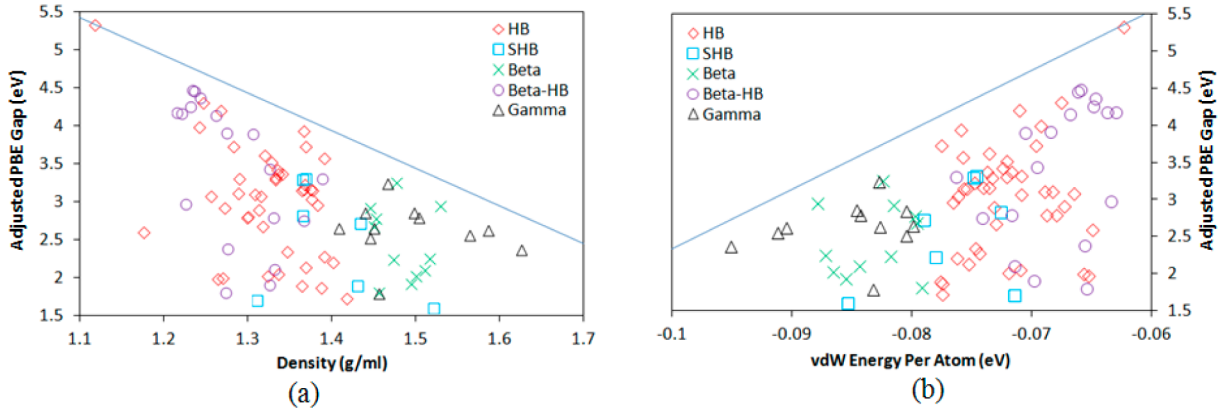

Figure 10. Predicted optical gaps as a function of density and vdW energy for PAHs. E_g^{PBE}in both panels a and b were calculated on PBE+vdW geometry optimized structures and adjusted with ξ_{PBE} to give the predicted E_g^{opt}. (a) Comparison of calculated densities and E_g^{opt}. Blue line represents the E_g^{opt}vs ρ limit. (b) vdW energy as a function of E_g^{opt}. Blue line represents the E_g^{opt} vs vdW energy per atom limit.

shows a direct relationship between the H···H contacts and the maximum E_g^{opt} value. When an E_g^{opt} boundary line is drawn as a function of H···H% using benzene and graphite as extrema (as done in Figure 9a), 99% of all PAH optical gaps will exist below the limiting function.

The inverse correlation of Figure 9a occurs because the C···C contacts are associated with $\pi\cdots\pi$ interactions and more efficient packing within crystalline PAHs. Therefore, an increase in the C···C contacts would increase the electrodynamic interaction of the π-electrons through increased overlap of neighboring molecules.[59] The positive correlation of Figure 9b can be explained by the fact that higher percentages of H···H contacts in PAHs are associated with inefficiencies in the molecular packing. This leads to less dense structures with weaker interactions between π-orbitals and therefore larger gaps.

It has been shown both experimentally[60−62] and theoretically[11] that the more dense a PAH crystal becomes (through high pressure), the smaller E_g becomes. This trend of decreasing E_g with increasing density also holds for ambient pressure PAH crystals. The blue line in Figure 10a exemplifies the fact that on average, the higher the density in the ambient pressure structures, the smaller the maximum possible E_g^{opt} will be. It is therefore no coincidence that the β and γ structures, which are among the densest on average, possess the smallest average maximum gaps.

When the predicted optical gaps and densities of benzene and HOPG are taken as limiting cases, there is an upper limit or ceiling that dictates how large E_g^{opt} can be for a PAH at a given density (ρ); the ceiling of the optical gap (E_g^{max}) as a function of ρ is represented by a blue line in Figure 10a and by eq 1:

$$E_g^{max}(\rho) = (-4.62\ \text{eV·mL/g})\rho + 10.50\ \text{eV} \quad (1)$$

Similarly, when E_{vdW} is plotted as a function of the predicted optical gap, a similar E_g^{max} scenario can be observed (see Figure 10b). For this limiting function, the optical gap and E_{vdW} for graphite and benzene are used as limiting cases. The line describing this limit is expressed as

$$E_g^{max}(E_{vdW}) = (68.28)E_{vdW} + 9.60\ \text{eV} \quad (2)$$

In Figures 9 and 10, a lower limit also appears to be present in the band gaps of *stable* PAH molecular crystals. Though it is known that the band gap of PAHs can be lowered below 1.5 eV through the substitution of hydrogen with halogens, chalcogens, and other "R-groups",[2] as well as expansion of the system via the addition of more rings (often leading to unstable configurations), all reported *stable* monomolecular PAH

dx.doi.org/10.1021/jp5064462 | J. Phys. Chem. C 2014, 118, 19964−19974

crystals appear to push down against a 1.5 eV lower limit. It is expected that larger discotic PAHs could be stable in the crystalline state and produce band gaps below 1.5 eV, but at present crystal structures of these materials have not been reported. Therefore, if the density, C···C%, or vdW energy of a PAH is known, one can expect the band gap to be above 1.5 eV and at or below the E_g^{max} ceiling of that variable.

3.4. Comparison of Crystalline and Molecular Optical Gaps. It is known that the energy needed for a system to excite an electron is reduced when going from the gas or solution state to the crystal because of stabilizing interactions within the crystal. This can be demonstrated by the fact that the E_g^{opt} of isolated molecules is always larger than that of the molecules in the crystal as shown in Figure 11. The difference between the

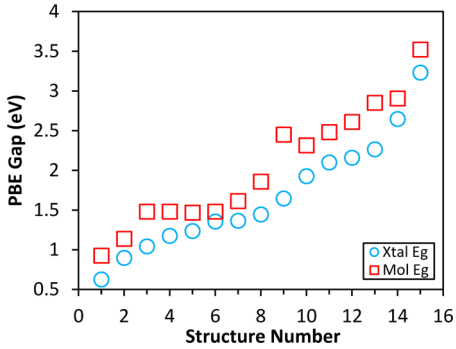

Figure 11. Comparison of E_g^{Xtal} and E_g^{Mol} as calculated with PBE. Values from Tables 1 and 2. Stuctures (1) QUATER10, (2) PENCEN, (3) QQQCIG04, (4) QQQCIG14, (5) POBPIG, (6) QQQCIG13, (7) TETCEN01. (8) PERLEN07, (9) HBZCOR, (10) ANTCEN, (11) BEANTR, (12) PYRENE02, (13) CORONE01, (14) TERPHE02, and (15) BIPHEN.

crystalline (Xtal) and molecular (Mol) band gaps ($\Delta E_g^{Xtal-Mol}$) can help describe the intermolecular interactions present in the crystal:

$$\Delta E_g^{Xtal-Mol} = E_g^{Xtal} - E_g^{Mol} \quad (3)$$

Comparison of the experimentally available $\Delta E_g^{Xtal-Mol}$ and those calculated with PBE are presented in Figure 12. While agreement between E_g^{opt} and E_g^{PBE} is good when adjusted with ξ_{PBE} (as shown in Figures 6 and 7) the numbers *do* vary slightly from experiment. Since $\Delta E_g^{Xtal-Mol}$ depends on both molecular and crystal E_g^{opt} values, if one or both are slightly off, then the $\Delta E_g^{Xtal-Mol}$ can deviate significantly from experiment (this is because variations between the E_g^{opt} and E_g^{PBE} are of the same order of magnitude as $\Delta E_g^{Xtal-Mol}$). So, while PBE produced several good $\Delta E_g^{Xtal-Mol}$ correlations with experiment in Figure 12 (namely, for structures 3, 4, 8, and 10), significant deviations exist for the remaining structures.

In order to obtain a more quantitative prediction of $\Delta E_g^{Xtal-Mol}$, we investigated whether higher level methods such as PBE0 could alleviate the error. Figure 12 shows that the use of a hybrid functional actually increases the error associated with calculating $\Delta E_g^{Xtal-Mol}$. In the case of PBE0, the increased error because E_g^{Mol} is normally predicted to be ~12% larger than the experimental gap, while the error associated with E_g^{Xtal} is smaller (5.6%). Therefore, when the difference between the two is taken, $\Delta E_g^{Xtal-Mol}$ is typically overestimated with respect to PBE values. To correctly predict $\Delta E_g^{Xtal-Mol}$, it will be necessary to employ higher level methods such as GW.

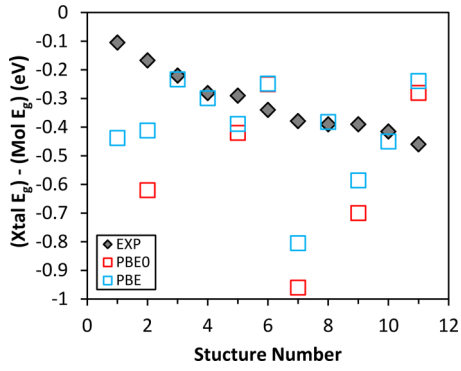

Figure 12. Comparison of experimental and calculated $\Delta E_g^{Xtal-Mol}$ for select PAHs. Values from Tables 1 and 2. Structures (1) QQQCIG04, (2) PERLEN07, (3) POBPIG, (4) QUATER10, (5) ANTCEN, (6) TETCEN01, (7) HBZCOR, (8) BEANTR, (9) CORONE01, (10) PYRENE02, and (11) PENCEN.

4. CONCLUSION

Dispersion inclusive DFT was used to model the structural and electronic properties of all PAHs available in the CSD. It was found that addition of a ~1 eV constant to the DFT-PBE gap provided good agreement with experiment optical gaps. Hirshfeld surface analysis revealed that relationships exist between the density, intermolecular cohesive energy, and relative fractions of C···C intermolecular contacts for the structures. Relationships between the close contact fractions and the optical gaps were also established; that is, limits in the maximum optical gaps of PAH crystals were established as a function of C···C close contact fractions. Similarly, it was demonstrated that a limit between the maximum optical gap and the intermolecular cohesive energy exists. An inverse correlation was found to exist between the density and maximum optical gap in these organic molecular crystals (OMC), where the β and γ motifs provide the smallest average optical gaps. A 1.5 eV minimum optical gap boundary was established for all *stable* PAH crystal structures currently available in the CSD. It was also shown that prediction of $\Delta E_g^{Xtal-Mol}$ needs a higher level theory than semilocal or hybrid functionals.

■ ASSOCIATED CONTENT

Supporting Information

List of CSD Refcodes and IUPAC structure names, list of calculated and experimental (1) unit cell parameters, (2) Hirshfeld surface close contact fractions, (3) π^0-parameter, (4) interplanar angle for all structures, and (5) molecular and crystalline E_g^{PBE}. This material is available free of charge via the Internet at http://pubs.acs.org.

■ AUTHOR INFORMATION

Corresponding Author

*E-mail: bxs54@psu.edu. Phone: 1 (724) 430-4257.

Notes

The authors declare no competing financial interest.

■ ACKNOWLEDGMENTS

This work was supported in part by the Eberly Science Fund and Grant NSF-DMR-1410736.

REFERENCES

(1) Anthony, J. E. The Larger Acenes: Versatile Organic Semiconductors. *Angew. Chem., Int. Ed.* **2008**, *47*, 452−483.
(2) Sun, Z.; Ye, Q.; Chi, C.; Wu, J. Low Band gap Polycyclic Hydrocarbons: from Closed-Shell Near Infrared Dyes and Semiconductors to Open-Shell Radicals. *Chem. Soc. Rev.* **2012**, *41*, 7857−7889.
(3) Kuc, A.; Heine, T.; Seifert, G. Structural and Electronic Properties of Graphene Nanoflakes. *Phys. Rev. B* **2010**, *81*, No. 085430.
(4) Malloci, G.; Cappellini, G.; Mulas, G.; Mattoni, A. Electronic and Optical Properties of Families of Polycyclic Aromatic Hydrocarbons: A Systematic (Time-Dependent) Density Functional Theory Study. *Chem. Phys.* **2011**, *384*, 19−27.
(5) Rieger, R.; Müllen, K. Forever Young: Polycyclic Aromatic Hydrocarbons as Model Cases for Structural and Optical Studies. *J. Phys. Org. Chem.* **2010**, *23*, 315−325.
(6) Burke, K. Perspective on Density Functional Theory. *J. Chem. Phys.* **2012**, *136*, No. 150901.
(7) Schatschneider, B.; Phelps, J.; Jezowski, S. A New Parameter for Classification of Polycyclic Aromatic Hydrocarbon Crystalline Motifs: A Hirshfeld Surface Investigation. *CrystEngComm* **2011**, *13*, 7216−7223.
(8) Desiraju, G. R.; Gavezzotti, A. From Molecular to Crystal Structure; Polynuclear Aromatic Hydrocarbons. *J. Chem. Soc., Chem. Commun.* **1989**, 621−623.
(9) Desiraju, G. R.; Gavezzotti, A. Crystal Structures of Polynuclear Aromatic Hydrocarbons. Classification, Rationalization and Prediction from Molecular Structure. *Acta Crystallogr., Sect. B: Struct. Sci.* **1989**, *45*, 473−482.
(10) McKinnon, J. J.; Jayatilaka, D.; Spackman, M. A. Towards Quantitative Analysis of Intermolecular Interactions with Hirshfeld Surfaces. *Chem. Commun.* **2007**, 3814−3816.
(11) Schatschneider, B.; Monaco, S.; Tkatchenko, A.; Liang, J.-J. Understanding the Structure and Electronic Properties of Molecular Crystals under Pressure: Application of Dispersion Corrected DFT to Oligoacenes. *J. Phys. Chem. A* **2013**, *117*, 8323−8331.
(12) Schatschneider, B.; Liang, J.-J.; Reilly, A.; Marom, N.; Zhang, G.-X.; Tkatchenko, A. Electrodynamic Response and Stability of Molecular Crystals. *Phys. Rev. B* **2013**, *87*, No. 060104.
(13) Schatschneider, B.; Liang, J. J. Simulated Pressure Response of Crystalline Indole. *J. Chem. Phys.* **2011**, *135*, No. 164508.
(14) Schatschneider, B.; Liang, J.-J.; Jezowski, S.; Tkatchenko, A. Phase Transition between Cubic and Monoclinic Polymorphs of the Tetracyanoethylene Crystal: The Role of Temperature and Kinetics. *CrystEngComm* **2012**, *14*, 4656−4663.
(15) Wolff, S. K.; Grimwood, D. J.; McKinnon, J. J.; Turner, M. J.; Jayatilaka, D. M.; Spackman, A. CrystalExplorer (version 3.0), University of Western Australia, 2012.
(16) Perdew, J. P.; Burke, K.; Ernzerhof, M. Generalized Gradient Approximation Made Simple. *Phys. Rev. Lett.* **1996**, *77*, 3865−3868.
(17) Tkatchenko, A.; Scheffler, M. Accurate Molecular Van Der Waals Interactions from Ground-State Electron Density and Free-Atom Reference Data. *Phys. Rev. Lett.* **2009**, *102*, No. 073005.
(18) Jain, A.; Hautier, G.; Ong, S. P.; Moore, C. J.; Fischer, C. C.; Persson, K. A.; Ceder, G. Formation Enthalpies by Mixing GGA and GGA + U Calculations. *Phys. Rev. B* **2011**, *84*, No. 045115.
(19) Jain, A.; Hautier, G.; Moore, C. J.; Ong, S. P.; Fischer, C. C.; Mueller, T.; Persson, K. A.; Ceder, G. A High-Throughput Infrastructure for Density Functional Theory Calculations. *Comput. Mater. Sci.* **2011**, *50*, 2295−2310.
(20) Spackman, M. A.; Jayatilaka, D. Hirshfeld Surface Analysis. *CrystEngComm* **2009**, *11*, 19−32.
(21) Heimel, G.; Puschnig, P.; Oehzelt, M.; Hummer, K.; Koppelhuber-Bitschnau, B.; Porsch, F.; Ambrosch-Draxl, C.; Resel, R. Chain-Length-Dependent Intermolecular Packing in Polyphenylenes: A High Pressure Study. *J. Phys.: Condens. Matter* **2003**, *15*, 3375−3389.
(22) Oehzelt, M.; Heimel, G.; Resel, R.; Puschnig, P.; Hummer, K.; Ambrosch-Draxl, C.; Takemura, K.; Nakayama, A. High Pressure X-Ray Study on Anthracene. *J. Chem. Phys.* **2003**, *119*, 1078−1084.
(23) Oehzelt, M.; Aichholzer, a.; Resel, R.; Heimel, G.; Venuti, E.; Della Valle, R. Crystal Structure of Oligoacenes Under High Pressure. *Phys. Rev. B* **2006**, *74*, No. 104103.
(24) Ruoff, R. S.; Thornton, T.; Smith, D. Density of Fullerene Containing Soot as Determined by Helium Pycnometry. *Chem. Phys. Lett.* **1991**, *186*, 456−458.
(25) Chung, D. D. L. Review of Graphite. *J. Mater. Sci.* **2002**, *37*, 1475−1489.
(26) Reilly, A. M.; Tkatchenko, A. Seamless and Accurate Modeling of Organic Molecular Materials. *J. Phys. Chem. Lett.* **2013**, *4*, 1028−1033.
(27) Otsuka, Y.; Tsukada, M. Theoretical Study of Crystal Structures and Energy Bands of Polyacene and Pentacene Derivatives. *J. Phys. Soc. Jpn.* **2009**, *78*, No. 024713.
(28) Sharifzadeh, S.; Biller, A.; Kronik, L.; Neaton, J. B. Quasiparticle and Optical Spectroscopy of the Organic Semiconductors Pentacene and PTCDA from First Principles. *Phys. Rev. B* **2012**, *85*, No. 125307.
(29) Biermann, D.; Schmidt, W. Diels-Alder Reactivity of Polycyclic Aromatic Hydrocarbons. 1. Acenes and Benzologs. *J. Am. Chem. Soc.* **1980**, *102*, 3163−3173.
(30) Lim, S.-H.; Bjorklund, T.; Spano, F.; Bardeen, C. Exciton Delocalization and Superradiance in Tetracene Thin Films and Nanoaggregates. *Phys. Rev. Lett.* **2004**, *92*, No. 107402.
(31) Ahn, T.-S.; Müller, A. M.; Al-Kaysi, R. O.; Spano, F. C.; Norton, J. E.; Beljonne, D.; Brédas, J.-L.; Bardeen, C. J. Experimental and Theoretical Study of Temperature Dependent Exciton Delocalization and Relaxation in Anthracene Thin Films. *J. Chem. Phys.* **2008**, *128*, No. 054505.
(32) Spano, F. C. The Spectral Signatures of Frenkel Polarons in H- and J-Aggregates. *Acc. Chem. Res.* **2010**, *43*, 429−439.
(33) Schwenn, P. E.; Burn, P. L.; Powell, B. J. Calculation of Solid State Molecular Ionisation Energies and Electron Affinities for Organic Semiconductors. *Org. Electron.* **2011**, *12*, 394−403.
(34) Nakayama, N.; Nagashima, U. Semiempirical Calculation of Electronic Spectra of Organic Compounds by Using the Improved Method of New-Γ Electron Repulsion Integral. Part 2. Polycyclic Aromatic Hydrocarbons (PAHs). *J. Mol. Struct.: THEOCHEM* **2003**, *640*, 25−37.
(35) Alvarez-Collado, J. R. On the Calculation of the Optical and Reactive Properties of the Polycyclic Aromatic Hydrocarbons (PAHs) by Using the Frozen Spin Molecular Orbital (SMO) Hartree-Fock (HF) Approach. *Int. J. Mod. Phys. B* **2010**, *24*, 5833−5846.
(36) Djurovich, P. I.; Mayo, E. I.; Forrest, S. R.; Thompson, M. E. Measurement of the Lowest Unoccupied Molecular Orbital Energies of Molecular Organic Semiconductors. *Org. Electron.* **2009**, *10*, 515−520.
(37) *Physical and Chemical Aspects of Organic Electronics*; Woll, C., Ed.; Wiley Publishing: Weinheim, Germany, 2009, 678 pp.
(38) Miteva, T.; Yakutkin, V.; Nelles, G.; Baluschev, S. Annihilation Assisted Upconversion: All-Organic, Flexible and Transparent Multicolour Display. *New J. Phys.* **2008**, *10*, No. 103002.
(39) Fetzer, J. Beyond Clar: The Use of Modern Analytical Tools for Large PAHs. *Polycyclic Aromatic Compounds* **1999**, *14&15*, 1−10.
(40) Clar, E.; Schmidt, W. Correlations between Photoelectron and UV Absorption Spectra of Polycyclic Hydrocarbons. The Pyrene Series. *Tetrahedron* **1979**, *35*, 1027−1032.
(41) Clar, E.; Schmidt, W. Correlations between Photoelectron and Ultraviolet Absorption Spectra of Polycyclic Hydrocarbons. The Perylene, Coronene and Bisanthene Series. *Tetrahedron* **1977**, *33*, 2093−2097.
(42) Maruyama, Y.; Iwaki, T.; Kajiwara, T.; Shirotami, I.; Inokuchi, H. Molecular Orientation and Absorption Spectra of Quaterrylene Evaporated Film. *Bull. Chem. Soc. Jpn.* **1970**, *43*, 1259−1261.
(43) Shirotani, I.; Inokuchi, H.; Akimoto, S. Effect of Pressure on Electrical and Optical Behaviour of Quaterrylene, $C_{40}H_{20}$. *Bull. Chem. Soc. Jpn.* **1967**, *40*, 2277−2280.

(44) Kurrle, D.; Pflaum, J. Exciton Diffusion Length in the Organic Semiconductor Diindenoperylene. *Appl. Phys. Lett.* **2008**, *92*, No. 133306.
(45) Broch, K.; Aufderheide, A.; Raimondo, L.; Sassella, A.; Gerlach, A.; Schreiber, F. Optical Properties of Blends: Influence of Mixing-Induced Disorder in Pentacene:Diindenoperylene versus Perfluoropentacene:Diindenoperylene. *J. Phys. Chem. C* **2013**, *117*, 13952−13960.
(46) Huang, L.; Liao, Q.; Shi, Q.; Fu, H.; Ma, J.; Yao, J. Rubrene Micro-Crystals from Solution Routes: Their Crystallography, Morphology and Optical Property. *J. Mater. Chem.* **2009**, *20*, 159−166.
(47) Bree, A.; Lyons, L. E. Photo- and Semi-Conductance of Organic Crystals. Part VI. Effect of Oxygen on the Surface Photo-Current and Some Photochemical Properties of Solid Anthracene. *J. Chem. Soc.* **1960**, 5206−5212.
(48) Najafov, H.; Lee, B.; Zhou, Q.; Feldman, L. C.; Podzorov, V. Observation of Long-Range Exciton Diffusion in Highly Ordered Organic Semiconductors. *Nat. Mater.* **2010**, *9*, 938−943.
(49) Mulder, B. J. Photoconductivity Spectra of Stable and Metastable Single Crystals of Perylene. *Recueil* **1965**, *84*, 713−728.
(50) Hochstrasser, R. M. The Crystal Spectrum of Perylene. *Can. J. Chem.* **1961**, *39*, 451−457.
(51) Sano, M.; Akamatu, H. Semiconductivity and Absorption Spectrum of Perylene single Crystals. *Bull. Chem. Soc. Jpn.* **1961**, *34*, 1569−1571.
(52) Proehl, H.; Toerker, M.; Sellam, F.; Fritz, T.; Leo, K.; Simpson, C.; Müllen, K. Comparison of Ultraviolet Photoelectron Spectroscopy and Scanning Tunneling Spectroscopy Measurements on Highly Ordered Ultrathin Films of Hexa-Peri-Hexabenzocoronene on Au(111). *Phys. Rev. B* **2001**, *63*, No. 205409.
(53) Brodin, M. S.; Soskin, M. S. Investigation of the Absorption Spectrum of a Single Crystal of 1,2-Benzanthracene in the Region of Lowest Electronic Transitions. *Opt. Spectrosc.* **1959**, *5*, 392−395.
(54) Ferguson, J. Absorption and Fluorescence Spectra of Crystalline Pyrene. *J. Chem. Phys.* **1958**, *28*, 765−768.
(55) Xiao, J.; Yang, H.; Yin, Z.; Guo, J.; Boey, F.; Zhang, H.; Zhang, Q. Preparation, Characterization, and Photoswitching/Light-Emitting Behaviors of Coronene Nanowires. *J. Mater. Chem.* **2011**, *21*, 1423−1427.
(56) Wakayama, N. I.; Matsuzaki, S.; Mizuno, M. UV Absorption Study of the Phase Transition in p-Terphenyl Crystals. *Chem. Phys. Lett.* **1980**, *75*, 587−589.
(57) Coffman, R.; McClure, D. S. The Electronic Spectra of Crystalline Toluene, Dienzyl, Diphenylmethane, and Biphenyl in the Near Ultraviolet. *Can. J. Chem.* **1958**, *36*, 48−58.
(58) Garcıa, N.; Esquinazi, P.; Barzola-Quiquia, J.; Dusari, S. Evidence for Semiconducting Behavior with a Narrow Band Gap of Bernal Graphite. *New J. Phys.* **2012**, *14*, No. 053015.
(59) Drickamer, H. G.; Frank, C. W. *Electronic Transitions and the High Pressure Chemistry and Physics of Solids*; Chapman and Hall: London, 1973.
(60) Farina, L.; Syassen, K.; Brillante, A.; Della Valle, R. G.; Venuti, E.; Karl, N. Pentacene at High Pressure. *High Press. Res.* **2003**, *23*, 349−354.
(61) Brillante, A.; Della Valle, R. G.; Farina, L.; Girlando, A.; Masino, M.; Venuti, E. Raman Phonon Spectra of Pentacene Polymorphs. *Chem. Phys. Lett.* **2002**, *357*, 32−36.
(62) Aust, R. B.; Bentley, W. H.; Drickamer, H. G. Behavior of Fused-Ring Aromatic Hydrocarbons at Very High Pressure. *J. Chem. Phys.* **1964**, *41*, 1856−1864.
(63) Baerends, E. J.; Gritsenko, O. V.; van Meer, R. The Kohn-Sham Gap, the Fundamental Gap and the Optical Gap: The Physical Meaning of Occupied and Virtual Kohn-Sham Orbital Energies. *Phys. Chem. Chem. Phys.* **2013**, *15*, 16408−16425.
(64) Malloci, G.; Mulas, G.; Cappellini, G.; Joblin, C. Time-Dependent Density Functional Study of the Electronic Spectra of Oligoacenes in the Charge States 1, 0, +1, and +2. *Chem. Phys.* **2007**, *340*, 43−58.